Laser induced crystallization of sputtered MoS$_2$ thin films

Alessandro Tonon [a,1], Enrico Di Russo [a,b,c,*,1], Francesco Sgarbossa [a,b], Luca Bacci [a], Nicola Argiolas [a], Carlo Scian [a], Yurii P. Ivanov [d], Giorgio Divitini [d], Brendan Sheehan [e], Davide De Salvador [a,b], Andrea Gasparotto [a], Vittorio Morandi [c], Ray Duffy [e], Enrico Napolitani [a,b,f,**]

[a] Università Degli Studi di Padova, Dipartimento di Fisica e Astronomia, via Marzolo 8, 35131, Padova, Italy
[b] Istituto Nazionale di Fisica Nucleare, Laboratori Nazionali di Legnaro, viale Dell'Università 2, 35020, Legnaro, (PD), Italy
[c] CNR-IMM, Via Gobetti 101, Bologna, 40129, Italy
[d] Electron Spectroscopy and Nanoscopy, Istituto Italiano di Tecnologia, Via Morego 30, Genova, 16163, Italy
[e] Tyndall National Institute, University College Cork, Lee Maltings, Cork, T12 R5CP, Ireland
[f] CNR-IMM, Via S. Sofia 64, 95123, Catania, Italy

ARTICLE INFO

ABSTRACT

The integration of transition metal dichalcogenides (TMDs) thin films into Si CMOS-based devices requires the development of new bottom-up material growth approaches producing high crystallinity films without affecting the SiO$_2$/Si substrate. For this purpose, sputtering is a suitable deposition method due to its simplicity, jointly with high reliability and large area deposition capabilities. However, sputtered layers are amorphous and require a post-deposition thermal treatment to obtain a highly crystalline film. Nanosecond pulsed laser annealing (PLA) has recently emerged as promising route to achieve large-scale crystalline TMDs films without significantly heating or affecting the underlying substrate. The aim of this work is to explore the possibility to produce crystalline 2H–MoS$_2$ on large areas directly on a SiO$_2$-on-Si substrate. The film structure, composition and morphology were monitored as a function of the laser pulse energy density by Raman spectroscopy, X-rays diffraction, Rutherford backscattered spectroscopy (RBS), scanning transmission electron microscopy (STEM) and atomic force microscopy (AFM). The electrical properties of the film with optimized crystallinity were finally investigated through deposition of Cr/Au contacts using shadow masks. This approach can be scaled to other TMDs materials and substrates, also paving the way for the fabrication of heterostructures and electrical devices on the top of a single substrate.

1. Introduction

Recently, two-dimensional (2D) transition metal dichalcogenides (TMDs) are gaining tremendous interest for their potential use in a wide number of applications, including nanoelectronics and photonics [1,2]. Among all the TMDs, the most studied and exploited is 2D molybdenum disulfide (MoS$_2$), due to its satisfying optoelectronic properties and promise for bio-applications like DNA, cancer, and Coronavirus detection [3]. Several approaches can be adopted to obtain crystalline MoS$_2$ multi-layers. Chemical vapor deposition (CVD) is promising compared to other growth methods, because it has proven to be effective for preparing large-area homogeneous films, presenting continuity and thickness uniformity [4]. Currently, a major effort is focused on paving the way for MoS$_2$ industrial-scale synthesis and direct integration into silicon-based CMOS technology at the back-end-of-line (BEOL). In order to do this, a growth methodology suitable to fabricate a wafer-scale layer maintaining the substrate temperature below 500 °C is required [5]. Unfortunately, low thermal budget CVD approaches ($<$500 °C) result in poor layer number control and the formation of isolated grains with very small lateral size [6]. On the other hand, high quality MoS$_2$ can be obtained using high growth temperatures (around 750 °C), making the film growth on the top of pre-existing heterostructures or devices difficult

[7]. Although alternative approaches to CVD have solved most of the major material quality limitations (e.g., molecular beam epitaxy; atomic layer deposition) [8–10], radio frequency magnetron sputtering (RFMS) has progressively emerged as reliable, fast and cheap deposition method [11,12]. In particular, room temperature RFMS followed by post-deposition thermal annealing at a higher temperature provides high quality crystalline MoS₂ layers comparable to those grown by CVD [13]. Several approaches were recently emerged as viable alternative to furnace annealing, including e-beam irradiation and laser annealing [14–16]. Among all these approaches, laser annealing is particular advantageous because it allows not only to process well-defined sample areas, but also to induce controlled chemical modifications in TMDs films, tuning their structural, optical and electrical properties [17].

Many examples of laser annealing of room-temperature sputtered films were reported in literature. In particular, early studies have focused on the use of continuous wave laser beam (514 nm) to obtain crystalline MoS₂ and WS₂ ultra-thin films (<10 nm thick) [18]. Afterwards, similar results were obtained changing the laser wavelengths or using pulsed sources, such as a 473 nm continuous-wave laser [19], a pulsed Nd:YVO3 laser (355 nm) [20] or a Nd:YAG laser (532 nm) [21]. Recently, the sequential use of different nano-second lasers to ablate a MoS₂ target (248 nm KrF laser with 20 ns pulse duration) and then crystallize the film deposited on substrates under Ar gas atmosphere (with a tuneable nanosecond 1064 nm laser) was also explored [22]. The crystallization of an amorphous MoS₂ film deposited by DC magnetron sputtering at room temperature was also observed using a nanosecond KrF laser (248 nm) operated in air [14]. This approach was successfully adopted for layers deposited on both flexible polydimethylsiloxane (PDMS) and SiO₂-on-Si substrates. Interestingly, due to strong surface localization of laser processes, the laser-induced crystallization of TMDs can be generally extended on a large variety of substrates, including SiO₂ [14], Si [23], glasses [19] and polymers [14,24].

This article reports about the capability of combining sputter deposition with nanosecond laser annealing to synthetize crystalline MoS₂ on the top of a SiO₂ layer, in air. In particular, the morphological, structural and electrical properties of MoS₂ films were investigated by varying the laser density of energy, in order to optimize the crystallization process.

2. Experimental section

2.1. Material used

MoS₂ amorphous films were deposit by RFMS on SiO₂-on-Si substrates. These substrates are (725 ± 25) μm thick Czochralski silicon wafer, oriented along <100>, presenting a (90 ± 4.5) nm thick thermally grown SiO₂ layer on both the wafer sides. Samples were cleaned with acetone, followed by an ultrasonic cleaning in isopropanol. A N₂ jet was then used to dry samples. Finally, samples have undergone 10 min UV/ozone cleaning. RFMS was performed using a MoS₂ target supplied by NanoVision (99.95% purity). In order to do this, the deposition chamber was evacuated down to about 1×10^{-6} mBar; afterwards, it was filled with Ar₂ gas, reaching a dynamic equilibrium pressure of 5×10^{-3} mBar (8.8 sccm flow). The deposition procedure consisted in a 90 s long power rising ramp of up to 40 W, followed by 1 min of pre-sputtering and 5 min of deposition.

The film thickness was firstly measured in control samples with a KLA Tencor P17 stylus profilometer, obtaining a thickness of (13.4 ± 1.4) nm. This value was verified by performing x-rays reflectivity (XRR) measurements (not showed here) using a Philips PANalytical X'Pert PRO diffractometer, resulting in a thickness of (14.0 ± 0.3) nm. The composition of the film was also evaluated by Rutherford backscattering spectrometry (RBS). Mo and S areal doses resulted to be $(20 \pm 2) \times 10^{15}$ atoms/cm² and $(38 \pm 6) \times 10^{15}$ atoms/cm², respectively. These results confirm the good stoichiometry of the amorphous film deposited, pointing out a S/Mo ratio equals to 2.3 ± 0.2, a value very closed to the expected stoichiometry (i.e., 2). Furthermore, the

equivalent film thickness is calculated considering elemental density for both Mo and S species, resulting in a (14 ± 1) nm thick layer. The consistency of the profilometer, XRR and RBS measurements confirms the formation of a uniform and compact film over cm-scale lengths.

Samples were therefore annealed immediately after the sputtering deposition to minimize air exposure and to prevent the material oxidation. Pulsed laser annealing (PLA) was performed using a Coherent COMPex201 KrF excimer laser (emission wavelength 248 nm, pulse duration 22 ns). The whole surface of each sample (2.0×1.5 cm²) was processed using a grid formed by identical 5×5 mm² laser spots, presenting an energy density (ED) equal to 75, 100, 125 or 150 mJ/cm² (ED spatial uniformity within 2%). The processes were performed in air with a constant N₂ flux of 10 L/min directed toward the sample surface.

The electrical properties of the laser processed MoS₂ films were tested by depositing metallic contacts directly on the top of them. In particular, a contact geometry compatible with the realization of top-gated field effect transistors (FETs) was adopted, leaving the realization of the complete device to the future. In order to do this, metallic contacts were fabricated using a shadow mask designed for the deposition of 20 contacts pairs, each one formed by a source and a drain contact. This mask allows to vary the conduction channel length (i.e., drain-source distance), using values of 10, 20, 30 and 50 μm, fixing the channel width to 1 mm. Metallic contacts were deposited by magnetron sputtering (deposition pressure of 1×10^{-6} mBar) and are formed by a ~30/80 nm thick Cr/Au stack. In particular, Cr was DC deposited at 50 W for 100 s; Au was deposited for 4 min at 30 W in RF mode. A schematic illustrating the main steps toward the fabrication of the final device layout (without top gate) is depicted in Fig. 1.

2.2. Characterization and measurements

Raman spectra were acquired using a Thermo Fisher Scientific DXR2 confocal Raman microscope, equipped with a diode-pumped solid-state (DPSS) laser producing a 532 nm light beam impinging at normal incidence on the sample surface (laser spot size ~ 1.1 μm) after passing through the 100× microscope objective. The spectra were obtained using an 1800 lines/mm grating in the range from 30 to 1889 cm⁻¹, where MoS₂ and Si substrate peaks are expected. Each spectrum was the result of the average of 20 consecutive exposures with an integration time of 3 s each. The laser power was fixed to 5 mW, in order to avoid sample heating or damaging. Grazing incidence X-rays diffraction (GIXRD) and reflectance (XRR) spectra were acquired using a Philips PANalytical X'Pert PRO diffractometer. RBS measurements were performed using a ^{4}He $^+$ beam at 2.0 MeV obtained by the AN2000 accelerator at INFN-LNL. Electrical measurements were performed in a probe station inserted in a Faraday cage and shielded from illumination. The devices driving voltages were provided by a Keithley Source Measure Unit (SMU). The same SMU achieved also current measurements with 0.1 nA accuracy. Morphological and structural characterizations were performed using atomic force microscopy (AFM), scanning electron microscopy (SEM) and transmission electron microscopy (TEM). Surface morphology maps were collected using a Veeco Autoprobe CP-II microscope operated in semi-contact mode using Nanosensor PPP-NCHR probes. Wide-field morphology images were acquired using a Zeiss Crossbeam500 SEM, operated at 10 kV. The same microscope was also used to prepare TEM lamella specimens. In order to do this, material chunks were lifted out in correspondence of the Cr/Au contacts using a Ga-focused ion beam (FIB) at 30 kV acceleration. Lamellae were then thinned down to ~80 nm thickness, and a final clean up procedure was performed using a 2 kV ion beam. STEM observations were performed using a double corrected Thermo Fisher Scientific Spectra 300 installed at IIT-Genova, operated at 300 kV. The microscope was equipped with a large area Bruker energy dispersion X-ray spectroscopy (EDS) system in Dual-X configuration, that allows an efficient determination of the elemental composition at the nm-scale.
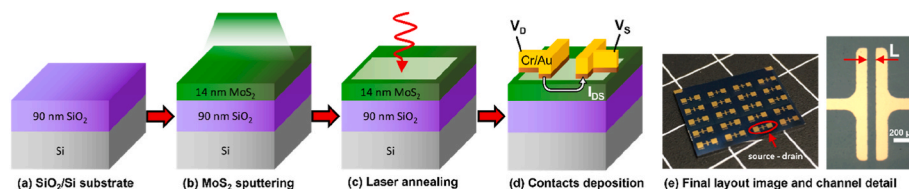
Fig. 1. Schematic representation of the FET fabrication sequence: (a) SiO$_2$-on-Si substrate. (b) MoS$_2$ sputtering deposition. (c) Pulsed laser annealing. (d) Cr/Au contact deposition. (e) Image of the final devices, without the top gate (the white grid has a 1 cm pitch) and detail of a device channel.

3. Results and discussion

In order to identify the optimal PLA conditions leading to the formation of crystalline MoS$_2$ layers, both Raman spectroscopy and XRD were performed on both reference (i.e., as-deposited) and laser processed samples. The evolution of Raman spectra as a function of the ED is illustrated in Fig. 2 a. Raman spectra exhibit a main peak at around 520 cm^{-1}, associated to the Si substrate. In addition, the two principal vibrational modes associated to the formation of 2H–MoS$_2$ can be identified in laser annealed samples, but only for ED $\geq$ 100 mJ/cm^2. Specifically, the in-plane vibration mode E_{2g}^1 appears around 383 cm^{-1}, while the out-of-plane vibration mode A_{1g}^1 is observed at about 410 cm^{-1}. The spectral distance between the two peaks is $\Delta k \approx 27$ cm^{-1}, which is quite close to the expected value for bulk-like MoS$_2$ films ($\Delta k = 26$ cm^{-1}), suggesting the formation of crystals with a number of layers
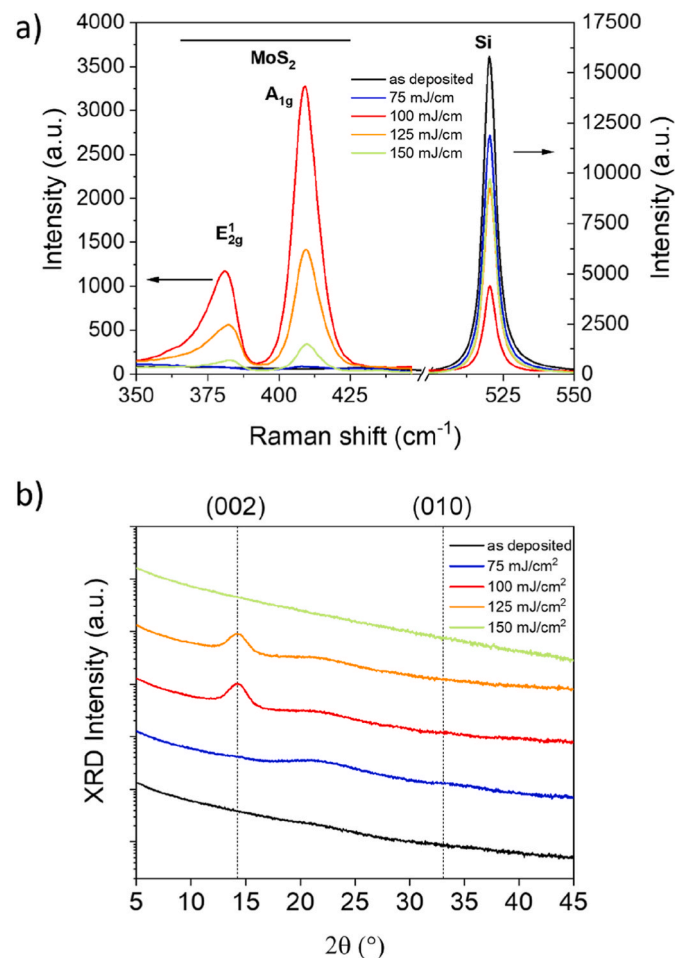

Fig. 2. (a) Raman and (b) XRD spectra as a function of the laser energy density (ED) after two laser pulses. Raman spectra are represented using the very same arbitrary unit reference system for both the spectral regions of interests (i.e., MoS$_2$ and Si peaks regions).

higher than 6 [25]. Nevertheless, the peaks distance measured is slightly greater than the expected one for a bulk-like material; this discrepancy is due to the shift of the E_{2g}^1 peak toward lower wavenumber of about 1 cm^{-1}, suggesting the presence of structural disorder [26]. Since the MoS$_2$ peaks distance remains almost unaltered varying the ED, an increase of the peak intensity has been interpreted in terms of improved material quality (i.e., crystallinity) due to more efficient laser processes. Additionally, no significant sample heating or damaging was pointed out during Raman measurements. In particular, the Si peak position fits the value expected for room temperature measurements (520 cm^{-1}) and no modification of the sample surface morphology was observed by the optical microscope.

XRD spectra provide further information about the MoS$_2$ film structure. The transition from an amorphous layer to 2H–MoS$_2$ leads to the formation of specific diffraction peaks. In particular, starting from ED = 100 mJ/cm^2, the rising of a diffraction peak at $2\theta = 14.25°$ suggests the formation of (002)-planes oriented parallel to the SiO$_2$ sample surface, as illustrated in Fig. 2 b. This XRD pattern doesn't show any other peaks that would be present in the case of a polycrystalline growth (such as a (010)-plane peaks). Instead, the (002) peak indicates a c-axis oriented growth of the MoS$_2$ film [13]. The (002)-peak broadening was used to calculate grain size, limited to the <002> direction, according to Scherrer equation. Starting from a 14 nm amorphous film, this size is of about (5.0 $\pm$ 0.5) nm, which corresponds to about 7–8 MoS$_2$ layers, thereby corroborating the values extracted from the Raman peak separation.

A comparison between Raman A_{1g}/Si peak height and XRD peak area (normalized) trend as a function of the laser ED is reported in Fig. 3 a. In both cases, the presence of a crystallization threshold for a laser ED = 100 mJ/cm^2, below which MoS$_2$ remains amorphous, is clearly apparent. In addition, two laser pulses performed at this threshold ED produce the best crystalline quality film. A further increase of the ED to 125 mJ/cm^2 leads to a deterioration of the material structure, ultimately leading to disappearance of both Raman and XRD peaks for the ED = 150 mJ/cm^2. Interestingly, the comparison of A_{1g}/Si peak intensity ratio obtained for the best PLA conditions (i.e., ED = 100 mJ/cm^2) with the values reported in Ref. [25] (including experimental data and theoretical calculations as a function of the number of MoS$_2$ layers) suggests the formation of 2–3 crystalline layers of MoS$_2$. Such a low number of layers could be unexpected, but can be explained by non-ideal coupling between stacked crystalline monolayers of MoS$_2$. In contrast with a few-layers of exfoliated film, the use of PLA to synthetize MoS$_2$ could introduce impurities, sulphur vacancies, point defects and staking faults that strongly modify the interlayer coupling and reduce the resulting vibrational amplitudes, leading to an underestimation of the number of crystalline layers.

The average composition of the MoS$_2$ layers before and after laser annealing was then assessed by using RBS. The areal doses measured for Mo and S are reported in Fig. 3 b. The Mo areal dose is almost constant after laser annealing, remaining close to the dose deposited that was (19.6 $\pm$ 1.5) $\times$ 10^{15} at/cm^2. Instead, the S areal dose was observed to significantly decrease after laser annealing, probably as a result of ablation phenomena in air, with a consequent reduction of the amount of S that can be incorporated in 2H–MoS$_2$ layers. This preferential loss of S atoms is clearly emphasized with increasing ED of the laser, even
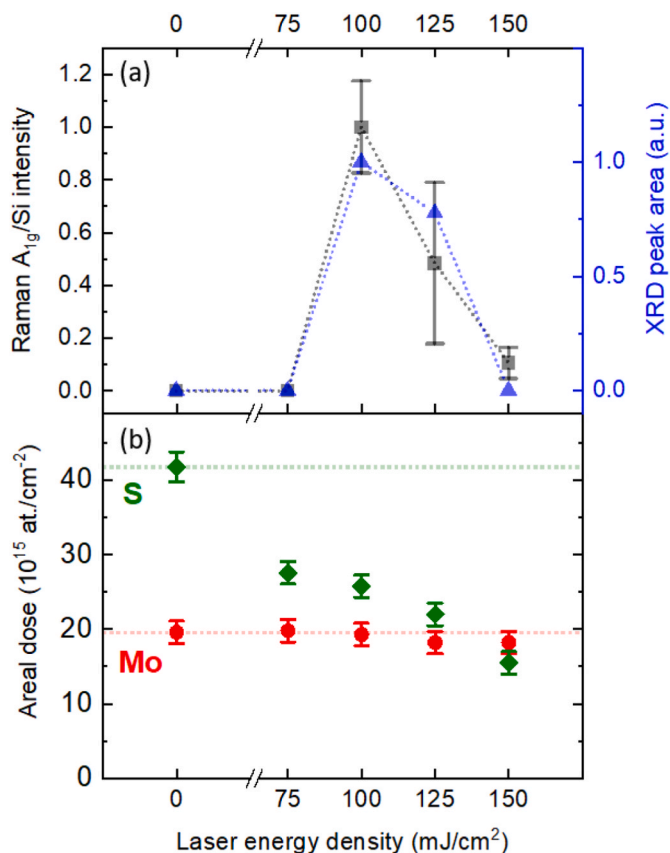
Fig. 3. (a) Raman peaks ratio A_{1g}/Si and normalized area of XRD (002)-peaks as a function of the laser ED. (b) RBS areal doses of Mo and S as a function of the laser ED (the red/green horizontal lines indicate the S/Mo areal dose deposited).

sample processed with laser ED = 100 mJ/cm^2, the equivalent crystal-line film thickness should be (6.9 ± 0.3) nm, corresponding to about 11 2H–MoS$_2$ monolayers. This thickness exceeds the estimate provided by Raman and XRD analyses. This result can be interpreted as indication of a non-uniform 2H–MoS$_2$ film, most likely also including non-crystalline regions. In order to obtain more details of both the morphology and the structure of the crystalline layers, AFM, SEM and high-resolution cross-section TEM micrographs were acquired.

The surface morphology of the sample processed with ED = 100 mJ/cm^2 was observed using both SEM and AFM. The presence of a micrometre-scale uniform MoS$_2$ layer was clearly revealed by SEM micrographs, as it can be observed in Fig. 4 a. The presence of a large number of bright circular nanometre-size spots on the sample surface was interpreted as the formation of bumps after performing laser annealing. This was corroborated by AFM morphology maps, that showed the formation of 15–30 nm height bumps presenting a diameter of about 20–40 nm, as illustrated in Fig. 4 b. The presence of these bumps leads to an increase of the surface roughness up to (11.4 ± 1.5) μm, while a roughness of about (0.10 ± 0.01) nm was measured for the as-deposited amorphous MoS$_2$ layer, confirming that after deposition the pristine layer was extremely flat, compact and homogeneous.

High-angle annular dark field scanning transmission electron microscopy (HAADF-STEM) images of the crystalline MoS$_2$ film cross sections were then acquired in order to observe the material after the deposition of metallic contacts. Selected images are reported in Fig. 4 c. MoS$_2$ forms a 5–8 nm thick layer presenting nanocrystals with (002)-planes preferentially oriented parallel to the SiO$_2$ substrate interface. Each nanocrystal is formed by about 4–8 layers presenting an interlayer distance of about 0.67 nm, thereby confirming the results previously obtained by Raman and XRD. STEM observations also enabled in-depth investigation of the bumps revealed by both SEM and AFM. In particular, EDS-STEM compositional maps indicate that these correspond to amorphous regions formed by Mo, S and O, as depicted in Fig. 4 d. We therefore believe that these bumps could host the excess of Mo not incorporated in MoS$_2$ nanocrystals and detected by the RBS measurements. The mechanism leading to the formation of these bumps has not been fully understood yet, but they could be ascribed to some local melting phenomena during PLA, leading to the creation of Mo-rich coalescences. Therefore, the average S-poor composition of these structures could promote the incorporation of O from the atmosphere, leading to the formation of MoO$_2$, whose presence has already been
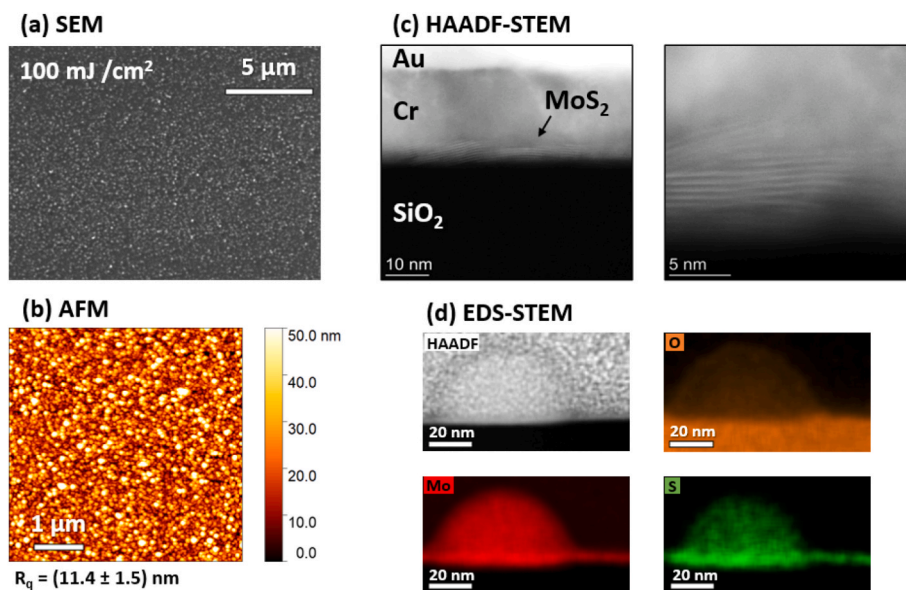
though there is no correlation between the average composition of the resulting layer and the material crystallinity. Finally, RBS data also allows to estimate an upper limit of the crystalline film thickness by considering the areal Mo and S doses (but neglecting the Mo surplus) and assuming the material density of a 2H–MoS$_2$. In the case of the

Fig. 4. (a) SEM and (b) AFM micrograph acquired from the surface of the sample processed at ED = 100 mJ/cm^2 (c) HAADF-STEM images of a SiO$_2$/MoS$_2$/Cr/Au stack(left) and a detail of the MoS$_2$ crystalline layer (right). (d) EDS-STEM compositional maps in correspondence of a surface bump.

observed in similar films by X-ray photoelectron spectroscopy (XPS) [27].

In order to study the electrical properties of MoS_2 films, current-voltage curves $I_{DS}(V_{DS})$ were acquired (see Fig. 1d). First of all, V_{DS} was varied in the range ± 10 V (where: V_{DS} is the potential difference between drain and source contacts; I_{DS} is the current flowing between these two contacts through the MoS_2 film). The MoS_2 films with no laser annealing (i.e., as-deposited) reveal no current flow (I_{DS}) in this voltage range (data not shown here). Instead, the MoS_2 films laser processed at ED = 100 mJ/cm^2 are electrically conductive. The $I_{DS}(V_{DS})$ curves obtained varying the channel lengths are reported in Fig. 5. Data indicate that an increase of the channel length L is associated to a reduction of the current I_{DS} for a given V_{DS}. In addition, the $I_{DS}(V_{DS})$ curves exhibit a linear trend in the range $V_{DS} = \pm 5$ V, suggesting the presence of non-rectifying contacts between Cr/Au and MoS_2 as expected from literature, where reports indicate that a thick Cr layer achieves better ohmic junction with respect to direct Au contacts [28]. In addition, the formation of MoO_x in correspondence of the film surface could also enhance this non-rectifying behaviour thanks to the high work function of MoO_x jointly with the possible reduction of mid-gap states leading to the Fermi level pinning [29]. The slope of the linear region is related to the total resistance of the device R_{TOT}, which in turn depends linearly on the channel length L, as shown in the inset of Fig. 4. In detail, $R_{TOT} = 2R_C + R_{MoS2}$, where R_{MoS2} is the MoS_2 channel resistance and R_C is the contact resistance of the device. This last quantity is independent of the channel length L. Therefore, R_C (and the associated error) can be easily calculated with a linear fit (see Fig. 5 inset), resulting to be $R_C = (5.96 \pm 0.56) \times 10^8$ Ω. Considering the contact geometry, the contact resistivity is $\rho_C = R_C L_T W$ where $L_T W$ represents the effective area where current flows under the metal contact [30]. In particular, the transfer length L_T is determined as the horizontal axis intercept of the linear fit in Fig. 5 inset, found to be $L_T = (11 \pm 1)$ μm. The resulting contact resistivity is $\rho_C = (6.63 \pm 0.01) \times 10^4$ Ω cm^2, which is comparable to those obtained for a large-area film [31]. Interestingly, the fabrication of high-quality metal/MoS_2 interface, leading to the formation of lower contact resistances, could be further improved by more stringent vacuum conditions (e.g., decreasing the vacuum deposition residual pressure down to 10^{-9} mBar) [32]. On the other hand, the metal/MoS_2 interface can also be altered by the presence of a thick Cr adhesion layer. In fact, Cr atoms can interact with the MoS_2 layer, causing its chemical reduction and forming both CrS_X and metallic Mo [1], increasing the number of defects. Lastly, Cr atoms deposition can also relocate Mo and S atoms toward the substrate, producing inhomogeneities at the interface [33]. However, TEM micrographs show no evident damaging effects due to the deposition of Cr on MoS_2 (see Fig. 4c). Considering the R_{MoS2} values for different channel lengths, it was possible to determine the average value of the sheet resistance of the MoS_2 film, which was estimated as $R_{SH} = (1.06 \pm 0.06) \times 10^{11}$ Ω/sq. Considering the previous estimates of about 10 crystallised MoS_2 layers, the material resistivity is $\rho_{MoS2} = (66 \pm 2)$ kΩ·cm. This value is one order of magnitude higher compared to those reported for similar non-intentionally doped MoS_2 layers grown by CVD followed by high temperature annealing [3]. This can be explained in terms of composition deviations from the expected stoichiometry (i.e., S-poor composition), which may lead to the formation of defects, especially sulphur vacancies [34]. In addition, the polycrystalline structure of the MoS_2 film with nanoscale grains results in the formation of boundaries that could further reduce film conductivity [30].

4. Conclusions

The UV pulsed laser annealing method applied on sputtered amorphous stoichiometric MoS_2 layer resulted in the crystallization of the film after 2 pulses performed at 100 mJ/cm^2. The resulting crystals structure was studied by AFM, SEM and TEM confirming the presence of nano-crystalline grains of 2H–MoS_2 and the formation of Mo-rich coalescences on sample surface. The optimized annealing conditions identified by Raman spectrometry and XRD were applied to investigate the electrical properties of the film. Cr/Au electric contacts were deposited on MoS_2 films by sputtering and I(V) characteristics were acquired in order to measure contact resistance, sheet resistivity and material resistivity. The measured contact resistance is comparable with the values found in literature, considering similar contacts fabrication methods. Instead, the material resistivity resulted to be higher compared to similar CVD growth films, suggesting lower crystal quality. In summary, this work shows that nano-second pulsed laser melting is a suitable method to produce crystalline MoS_2 layers on SiO$_2$-on-Si substrates. The method could be further optimized in future investigations to understand and control S evaporation and Mo-rich coalescences. With additional micro-fabrication steps, it can also be extended to the fabrication of MoS_2-based top-gated FETs over large-scale films. This device fabrication approach also represents a possible low-cost method for boosting the industrial applications of 2D materials over different substrates.

CRediT authorship contribution statement

Alessandro Tonon: Investigation, Formal analysis, Conceptualization, Writing – original draft. **Enrico Di Russo:** Writing – original draft, Investigation, Formal analysis, Conceptualization. **Francesco Sgarbossa:** Investigation, Formal analysis. **Luca Bacci:** Methodology. **Nicola Argiolas:** Methodology. **Carlo Scian:** Methodology. **Yurii P. Ivanov:** Investigation, Formal analysis. **Giorgio Divitini:** Supervision, Methodology, Formal analysis. **Brendan Sheehan:** Supervision, Methodology, Formal analysis. **Davide De Salvador:** Supervision, Methodology, Formal analysis. **Andrea Gasparotto:** Methodology. **Vittorio Morandi:** Supervision, Methodology. **Ray Duffy:** Supervision, Methodology, Formal analysis. **Enrico Napolitani:** Supervision, Resources, Project administration, Methodology.
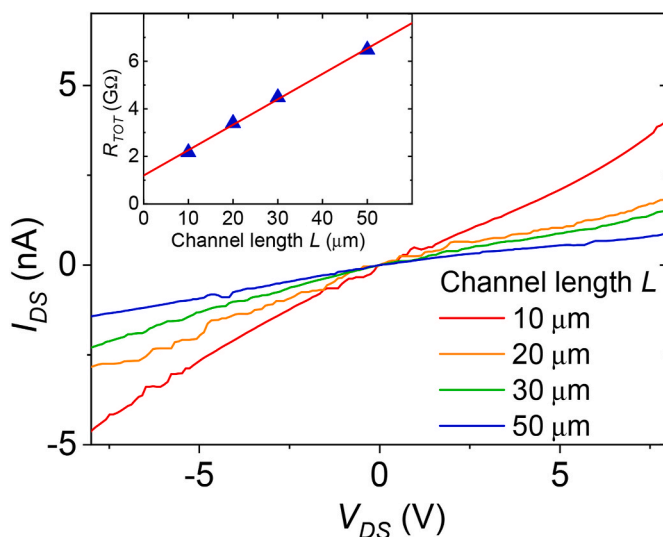

Fig. 5. Representative $I_{DS}(V_{DS})$ curves as a function of the channel length L. The total electrical resistance R_{TOT} for each curve is calculated as the inverse of the slope of the linear fit performed in the range $V_{DS} = \pm 5$ V. R_{TOT} as a function of the channel length L is represented in the inset.

Declaration of competing interest

The authors declare that they have no known competing financial interests or personal relationships that could have appeared to influence the work reported in this paper.

Data availability

Data will be made available on request.

References

[1] M. Samadi, N. Sarikhani, M. Zirak, H. Zhang, H.L. Zhang, A.Z. Moshfegh, Group 6 transition metal dichalcogenide nanomaterials: synthesis, applications and future perspectives, Nanoscale Horizons 3 (2018) 90–204, https://doi.org/10.1039/c7nh00137a.

[2] O. Samy, Z. Shuwen, M.D. Birowosuto, A. El Moutaouakil, A review on MoS2 properties, synthesis, sensing applications and challenges, Crystals 11 (2021) 355, 2021, https://www.mdpi.com/2073-4352/11/4/355.

[3] J. Lin, S. Monaghan, N. Sakhuja, F. Gity, R.K. Jha, E.M. Coleman, J. Connolly, C. P. Cullen, L.A. Walsh, T. Mannarino, M. Schmidt, B. Sheehan, G.S. Duesberg, N. McEvoy, N. Bhat, P.K. Hurley, I.M. Povey, S. Bhattacharjee, Large-area growth of MoS2 at temperatures compatible with integrating back-end-of-line functionality, 2D Mater. 8 (2021), https://doi.org/10.1088/2053-1583/abc460.

[4] Q. Ji, Y. Zheng, Y. Zhang, Z. Liu, Chemical vapour deposition of group-VIB metal dichalcogenide monolayers: engineered substrates from amorphous to single crystalline, Chem. Soc. Rev. 44 (2015) 2587–2602, https://doi.org/10.1039/c4cs00258j.

[5] J. Lin, S. Monaghan, N. Sakhuja, F. Gity, R.K. Jha, E. Coleman, J. Connolly, C. Cullen, L. Walsh, T. Mannarino, M. Schmidt, B. Sheehan, G. Duesberg, N. Mc Evoy, N. Bhat, P. Hurley, I. Povey, S. Bhattacharjee, Chemical Vapor Deposition of MoS2 for Back-End-Of-Line Applications, ECS Meet. Abstr. MA2021-02, 2021, p. 1952, https://doi.org/10.1149/MA2021-02311952mtgabs, 1952.

[6] A. Kozhakhmetov, R. Torsi, C.Y. Chen, J.A. Robinson, Scalable low-temperature synthesis of two- dimensional materials beyond graphene Journal of Physics : materials OPEN ACCESS Scalable low-temperature synthesis of two-dimensional materials beyond graphene, J. Phys. Mater. 4 (2020), 0–16.

[7] A.S. Pawbake, M.S. Pawar, S.R. Jadkar, D.J. Late, Large area chemical vapor deposition of monolayer transition metal dichalcogenides and their temperature dependent Raman spectroscopy studies, Nanoscale 8 (2016) 3008–3018, https://doi.org/10.1039/c5nr07401k.

[8] T.H. Choudhury, X. Zhang, Z.Y. Al Balushi, M. Chubarov, J.M. Redwing, Epitaxial growth of two-dimensional layered transition metal dichalcogenides, Annu. Rev. Mater. Res. 50 (2020) 155–177, https://doi.org/10.1146/annurev-matsci-090519-113456.

[9] L.K. Tan, B. Liu, J.H. Teng, S. Guo, H.Y. Low, K.P. Loh, Atomic layer deposition of a MoS2 film, Nanoscale 6 (2014) 10584–10588, https://doi.org/10.1039/c4nr02451f.

[10] S. Cadot, O. Renault, M. Frégnaux, D. Rouchon, E. Nolot, K. Szeto, C. Thieuleux, L. Veyre, H. Okuno, F. Martin, E.A. Quadrelli, A novel 2-step ALD route to ultrathin MoS2 films on SiO2 through a surface organometallic intermediate, Nanoscale 9 (2017) 538–546, https://doi.org/10.1039/c6nr06021h.

[11] G. Bräuer, B. Szyszka, M. Vergöhl, R. Bandorf, Magnetron sputtering - milestones of 30 years, Vacuum 84 (2010) 1354–1359, https://doi.org/10.1016/j.vacuum.2009.12.014.

[12] M. Acar, E. Gür, Sputtered 2D transition metal dichalcogenides: from growth to device applications, Turk. J. Phys. 45 (2021) 131–147, https://doi.org/10.3906/fiz-2104-8.

[13] H. Samassekou, A. Alkabsh, M. Wasala, M. Eaton, A. Walber, A. Walker, O. Pitkänen, K. Kordas, S. Talapatra, T. Jayasekera, D. Mazumdar, Viable route towards large-area 2D MoS2 using magnetron sputtering, 2D Mater. 4 (2017), https://doi.org/10.1088/2053-1583/aa5290.

[14] B. Sirota, N. Glavin, A.A. Voevodin, Room temperature magnetron sputtering and laser annealing of ultrathin MoS2 for flexible transistors, Vacuum 160 (2019) 133–138, https://doi.org/10.1016/j.vacuum.2018.10.077.

[15] R. Kaindl, B.C. Bayer, R. Resel, T. Müller, V. Skalova, G. Habler, R. Abart, A. S. Cherevan, D. Eder, M. Blatter, F. Fischer, J.C. Meyer, D.K. Polyushkin, W. Waldhauser, Growth, structure and stability of sputter-deposited MoS2 thin films, Beilstein J. Nanotechnol. 8 (2017) 1115–1126, https://doi.org/10.3762/bjnano.8.113.

[16] B.H. Kim, H.H. Gu, Y.J. Yoon, Large-area and low-temperature synthesis of few-layered WS2 films for photodetectors, 2D Mater. 5 (2018), https://doi.org/10.1088/2053-1583/aadef8.

[17] T. Afaneh, P.K. Sahoo, I.A.P. Nobrega, Y. Xin, H.R. Gutiérrez, Laser-assisted chemical modification of monolayer transition metal dichalcogenides, Adv. Funct. Mater. 28 (2018), https://doi.org/10.1002/adfm.201802949.

[18] M.E. McConney, N.R. Glavin, A.T. Juhl, M.H. Check, M.F. Durstock, A.A. Voevodin, T.E. Shelton, J.E. Bultman, J. Hu, M.L. Jespersen, M.K. Gupta, R.D. Naguy, J. G. Colborn, A. Haque, P.T. Hagerty, R.E. Stevenson, C. Muratore, Direct synthesis of ultra-thin large area transition metal dichalcogenides and their heterostructures on stretchable polymer surfaces, J. Mater. Res. 31 (2016) 967–974, https://doi.org/10.1557/jmr.2016.36.

[19] J.K. Wuenschell, H. Helvajian, Enhanced laser crystallization of thin film amorphous molybdenum disulfide (MoS 2) by means of pulsed laser ultrasound, Opt Express 27 (2019) 5859, https://doi.org/10.1364/oe.27.005859.

[20] J.K. Wuenschell, A.B. Payton, J.R. Lince, H. Helvajian, Laser processing of thin film sputtered MoS2: thinning, oxidation, and crystallization, J. Appl. Phys. 127 (2020), https://doi.org/10.1063/1.5112785.

[21] R.H. Rai, A. Pérez-Pacheco, R. Quispe-Siccha, N.R. Glavin, C. Muratore, Pulsed laser annealing of amorphous two-dimensional transition metal dichalcogenides, J. Vac. Sci. Technol. A 38 (2020), 052201, https://doi.org/10.1116/6.0000253.

[22] Z. Ahmadi, B. Yakupoglu, N. Azam, S. Elafandi, M. Mahjouri-Samani, Self-limiting laser crystallization and direct writing of 2D materials, Int. J. Extrem. Manuf. 1 (2019), https://doi.org/10.1088/2631-7990/ab0edc.

[23] C. Tessarek, O. Gridenco, M. Wiesing, J. Müssener, S. Figge, K. Sebald, J. Gutowski, M. Eickhoff, Controlled laser-thinning of MoS2Nanolayers and transformation to amorphous MoOx for 2D monolayer fabrication, ACS Appl. Nano Mater. 3 (2020) 7490–7498, https://doi.org/10.1021/acsanm.0c01104.

[24] R.H. Kim, J. Leem, C. Muratore, S.W. Nam, R. Rao, A. Jawaid, M. Durstock, M. McConney, L. Drummy, R. Rai, A. Voevodin, N. Glavin, Photonic crystallization of two-dimensional MoS2 for stretchable photodetectors, Nanoscale 11 (2019) 13260–13268, https://doi.org/10.1039/c9nr02173f.

[25] S.L. Li, H. Miyazaki, H. Song, H. Kuramochi, S. Nakaharai, K. Tsukagoshi, Quantitative Raman spectrum and reliable thickness identification for atomic layers on insulating substrates, ACS Nano 6 (2012) 7381–7388, https://doi.org/10.1021/nn3025173.

[26] S. Mignuzzi, A.J. Pollard, N. Bonini, B. Brennan, I.S. Gilmore, M.A. Pimenta, D. Richards, D. Roy, Effect of disorder on Raman scattering of single-layer Mo S2, Phys. Rev. B Condens. Matter 91 (2015) 1–7, https://doi.org/10.1103/PhysRevB.91.195411.

[27] B. Sirota, N. Glavin, A.A. Voevodin, Room temperature magnetron sputtering and laser annealing of ultrathin MoS2 for flexible transistors, Vacuum 160 (2019) 133–138, https://doi.org/10.1016/j.vacuum.2018.10.077.

[28] H. Yang, S. Cai, Y. Zhang, D. Wu, X. Fang, Enhanced electrical properties of lithography-free fabricated MoS2Field effect transistors with chromium contacts, J. Phys. Chem. Lett. 12 (2021) 2705–2711, https://doi.org/10.1021/acs.jpclett.1c00231.

[29] A. Rai, H.C.P. Movva, A. Roy, D. Taneja, S. Chowdhury, S.K. Banerjee, Progress in Contact, Doping and Mobility Engineering of MoS2: an Atomically Thin 2D Semiconductor, 2018, https://doi.org/10.3390/cryst8080316.

[30] G.K. Reeves, H.B. Harrison, Obtaining the specific contact resistance from transmission line model measurements, IEEE Electron. Device Lett. 3 (1982) 111–113, https://doi.org/10.1109/EDL.1982.25502.

[31] X. Song, W. Zan, H. Xu, S. Ding, P. Zhou, W. Bao, D.W. Zhang, A novel synthesis method for large-area MoS2 film with improved electrical contact, 2D Mater. 4 (2017), https://doi.org/10.1088/2053-1583/aa630f.

[32] C.D. English, G. Shine, V.E. Dorgan, K.C. Saraswat, E. Pop, Improved contacts to MoS2 transistors by ultra-high vacuum metal deposition, Nano Lett. 16 (2016) 3824–3830, https://doi.org/10.1021/acs.nanolett.6b01309.

[33] C. Kim, K.Y. Lee, I. Moon, S. Issarapanacheewin, W.J. Yoo, Metallic contact induced van der Waals gap in a MoS2 FET, Nanoscale 11 (2019) 18246–18254, https://doi.org/10.1039/c9nr04567h.

[34] M.I. Serna, S.H. Yoo, S. Moreno, Y. Xi, J.P. Oviedo, H. Choi, H.N. Alshareef, M. J. Kim, M. Minary-Jolandan, M.A. Quevedo-Lopez, Large-area deposition of MoS2 by pulsed laser deposition with in situ thickness control, ACS Nano 10 (2016) 6054–6061, https://doi.org/10.1021/acsnano.6b01636.